

# A Bayesian technique for improving the sensitivity of the atmospheric neutrino L/E analysis

A. S. T. Blake<sup>a,\*</sup>, J. D. Chapman<sup>a</sup>, M. A. Thomson<sup>a</sup>

<sup>a</sup>*Cavendish Laboratory, JJ Thomson Avenue, Cambridge, CB3 0HE, United Kingdom*

---

## Abstract

This paper outlines a method for improving the precision of atmospheric neutrino oscillation measurements. One experimental signature for these oscillations is an observed deficit in the rate of  $\nu_\mu$  charged-current interactions with an oscillatory dependence on  $L_\nu/E_\nu$ , where  $L_\nu$  is the neutrino propagation distance, and  $E_\nu$  is the neutrino energy. For contained-vertex atmospheric neutrino interactions, the  $L_\nu/E_\nu$  resolution varies significantly from event to event. The precision of the oscillation measurement can be improved by incorporating information on  $L_\nu/E_\nu$  resolution into the oscillation analysis. In the analysis presented here, a Bayesian technique is used to estimate the  $L_\nu/E_\nu$  resolution of observed atmospheric neutrinos on an event-by-event basis. By separating the events into bins of  $L_\nu/E_\nu$  resolution in the oscillation analysis, a significant improvement in oscillation sensitivity can be achieved.

*Keywords:* Neutrino oscillations, atmospheric neutrinos

---

## 1. Introduction

It has now been firmly established by experiment that atmospheric neutrinos undergo oscillations between flavours. In the standard theory, the oscillations arise from quantum mechanical mixing between the neutrino flavour eigenstates. This is governed by a unitary PMNS mixing matrix [1–3], which can be parameterised using three mixing angles and a CP-violating phase. The amplitudes of the oscillations depend on the sizes of the mixing angles, whereas the wavelengths depend on the neutrino squared-mass splittings,  $\Delta m_{ji}^2 = m_j^2 - m_i^2$ , and also on  $L_\nu/E_\nu$ , where  $L_\nu$  is the neutrino propagation distance and  $E_\nu$  is the neutrino energy.

The observed atmospheric neutrino  $\nu_\mu$  data are presently well-described by an effective two-flavour model of vacuum oscillations. In this approximation, the survival probability of an initial state  $|\nu_\mu\rangle$  is given by:

$$P(\nu_\mu \rightarrow \nu_\mu) = 1 - \sin^2 2\theta \sin^2 \left( \frac{1.27 \Delta m^2 (\text{eV}^2) L_\nu (\text{km})}{E_\nu (\text{GeV})} \right) \quad (1)$$

The two-flavour oscillation parameters,  $\Delta m^2$  and  $\sin^2 2\theta$ , have been measured in atmospheric neutrinos by a number of experiments, including Super-Kamiokande [4–6], MACRO [7], Soudan 2 [8] and MINOS [9–11]. In addition, the atmospheric neutrino results have been confirmed by the K2K [12], MINOS [13–15] and T2K [16] long-baseline experiments, using accelerator beams of muon neutrinos. The MINOS experiment reports confidence limits of  $|\Delta m^2| = (2.32^{+0.12}_{-0.08}) \times 10^{-3} \text{eV}^2$  (68% C.L.) and  $\sin^2 2\theta > 0.90$  (90% C.L.) [15].

For atmospheric neutrino experiments, one signature of neutrino oscillations is a deficit in the observed rate of  $\nu_\mu$  charged-current (CC) interactions relative to the prediction without oscillations. The size of the deficit varies with  $L_\nu/E_\nu$  according to the formula given in Eq. 1. The  $\nu_\mu$  CC interactions are identified by the presence of an emitted muon, which may also be accompanied by additional shower activity produced by the final-state hadronic system. The neutrino kinematics can be reconstructed by combining measurements of the emitted muon and hadronic system, obtained by analysing the observed hits in the detector. This yields measured values for the neutrino energy,  $E_\nu$ , and zenith angle,  $\theta_\nu$ . The reconstructed zenith an-

---

\*Corresponding author

gle is converted into a propagation distance,  $L_\nu$ , using a model of atmospheric neutrino production height.

The precision with which an atmospheric neutrino experiment can measure the oscillation parameters is dependent on its resolution of the neutrino energy and direction. Typically, the energy and direction of the muon can be measured precisely. However, the measurement of the hadronic system has a worse resolution. Therefore, the resolution of both  $E_\nu$  and  $\theta_\nu$  improves with  $E_\mu/E_\nu$ , where  $E_\mu$  is the muon energy. The angular resolution also improves with neutrino energy since the final-state particles are increasingly aligned with the incident neutrino direction. This is particularly important when the reconstructed muon direction is used to approximate the neutrino direction. The overall resolution is dependent on the precise configuration of the detector geometry. For example, the resolution is worse if there are fewer hits in the detector, or if the final-state particles are not fully contained in the detector.

The resulting resolution of  $L_\nu/E_\nu$  varies significantly across the  $\nu_\mu$  CC data sample. For the measurement of  $E_\nu$ , the resolution is worse for neutrino interactions with higher inelasticity, since the muon kinematics are better measured than those of the hadronic system. For the measurement of  $L_\nu$ , the resolution is worse at lower neutrino energies, where the average scattering angle between the neutrino and muon is larger, and also worse at the horizon, where  $L_\nu$  varies rapidly as a function of zenith angle, so that a small uncertainty in  $\theta_\nu$  translates into a significant uncertainty in  $L_\nu$ .

The oscillation sensitivity can be improved by incorporating information on the  $L_\nu/E_\nu$  resolution into the oscillation analysis. An example of this technique is the Super-Kamiokande L/E analysis [4], which uses a Monte Carlo simulation to calculate the average  $L_\nu/E_\nu$  resolution on a 2D grid of reconstructed neutrino energy and zenith angle. A sample of high resolution events is then selected by cutting out the regions of energy and angle with an average resolution less than 70%. The resulting  $L_\nu/E_\nu$  distribution of selected events is seen to exhibit a characteristic neutrino oscillation dip.

This paper describes a Bayesian technique for estimating the  $L_\nu/E_\nu$  resolution of atmospheric  $\nu_\mu$  and  $\bar{\nu}_\mu$  neutrinos on an event-by-event basis. For each event, a probability distribution function (PDF) in  $\log_{10}(L_\nu/E_\nu)$  is calculated by combining the measured properties of the emitted muon and

hadronic system in the event with a Monte Carlo simulation of the atmospheric neutrino spectrum, neutrino interaction kinematics, and detector resolution. The  $L_\nu/E_\nu$  resolution is then taken as the RMS of this PDF. In the oscillation analysis, all selected atmospheric neutrino events are included, with events binned according to their resolution.

The Bayesian technique is demonstrated using a simulated atmospheric neutrino data set from the MINOS experiment. For the MINOS atmospheric neutrino analysis, the separation of events into bins of  $L_\nu/E_\nu$  resolution is found to yield a significant improvement in the oscillation sensitivity.

## 2. MINOS Simulation and Reconstruction

The MINOS Far Detector [17] is a 5.4 kton tracking calorimeter located 705 m underground in the Soudan mine, MN, USA. Its large mass and underground location enable MINOS to measure atmospheric  $\nu_\mu$  and  $\bar{\nu}_\mu$  disappearance due to neutrino oscillations. Atmospheric neutrino  $\nu_\mu$  and  $\bar{\nu}_\mu$  CC interactions in the MINOS detector are identified by the presence of a muon track with a contained-vertex or an upward-going trajectory. The detector is also magnetised, allowing muon charge-sign to be determined from track curvature. This information is used to distinguish between  $\nu_\mu + N \rightarrow \mu^- + X$  and  $\bar{\nu}_\mu + N \rightarrow \mu^+ + X$  CC interactions.

The analysis presented here uses simulated contained-vertex atmospheric neutrino interactions in the MINOS detector. The MINOS Monte Carlo simulation uses the Bartol 3D [18] calculation of atmospheric neutrino fluxes and the NEUGEN [19] model of neutrino cross-sections. A GEANT3 [20] detector simulation tracks the final-state particles and provides a full description of the detector response and readout. The simulation is used to generate a sample of contained-vertex atmospheric neutrino interactions corresponding to a total exposure of 193,000 kton-years.

A series of dedicated algorithms are used to reconstruct the muon tracks and hadronic showers on the assumption that they are produced by atmospheric neutrino interactions [21]. For muon tracks, the propagation direction of the muon along the track is first determined using timing information. A Kalman Filter algorithm is then used to determine the muon trajectory through the detector [22]. For fully contained muons, which stop in the detector, the muon momentum is calculated from the track range; for partially contained muons, which

exit the detector, the momentum is calculated from the track curvature. For reconstructed showers, the total hadronic energy is calculated from the visible energy in the shower.

The atmospheric neutrino energy and direction are calculated from the reconstructed muon track and hadronic shower. The neutrino energy is taken to be the sum of the muon and shower energy; and the neutrino direction is taken to be the muon direction. The neutrino propagation distance is calculated by assuming a fixed 15 km neutrino production height in the atmosphere.

A set of selection requirements are applied that identify contained-vertex muon tracks produced by atmospheric neutrino interactions [23]. This yields a sample of 5.2 million simulated events which are used for this analysis. The  $\nu_\mu$  and  $\bar{\nu}_\mu$  CC component forms 94% of the selected sample of events, with the remaining 6% composed of the NC and  $\nu_e + \bar{\nu}_e$  CC backgrounds, which do not oscillate in the two-flavour model. The predicted event rates in the MINOS detector are 27 events per kton-year in the absence of oscillations, and 19 events per kton-year using representative oscillation parameters of  $|\Delta m^2| = 2.32 \times 10^{-3} \text{eV}^2$  and  $\sin^2 2\theta = 1.0$ , which are assumed throughout this paper.

Fig. 1 shows the true and reconstructed  $\log_{10}(L_\nu/E_\nu)$  distributions, plotted with and without oscillations, for those atmospheric neutrinos that pass the selection cuts. For these plots, and throughout this paper, the quantities  $L_\nu$  and  $E_\nu$  are measured in units of km and GeV, respectively. In the true oscillated distribution, there is a clear dip at  $\log_{10}(L_\nu/E_\nu) \approx 2.7$ , corresponding to the initial oscillation maximum, and a clear oscillatory structure at higher values of  $\log_{10}(L_\nu/E_\nu)$ . In the reconstructed distribution, the oscillations are smeared by detector resolution, with only the first oscillation dip clearly visible.

### 3. Bayesian L/E Analysis

The aim of the Bayesian analysis is to calculate a PDF in  $\log_{10}(L/E)$  for each event, based on its observed kinematics. For MINOS atmospheric neutrinos, these kinematic observables are: the reconstructed muon energy,  $E_\mu^R$ , and muon direction,  $\hat{p}_\mu^R$ ; and the reconstructed shower energy,  $E_{shw}^R$ . Each event is also tagged as  $q_\nu^R = (\nu_\mu, \bar{\nu}_\mu)$ , as determined by the reconstructed muon charge-sign. The corresponding true values for these variables are denoted  $E_\mu$ ,  $\hat{p}_\mu$ ,  $E_{shw}$  and  $q_\nu$  respectively.

The required PDF,  $P$ , can be written as follows:

$$P = P(\hat{p}_\nu, E_\nu, q_\nu | \hat{p}_\mu^R, E_\mu^R, E_{shw}^R, q_\nu^R), \quad (2)$$

where  $\hat{p}_\nu$  is the neutrino direction, which can be converted into the propagation distance,  $L_\nu$ .

Using Bayes' theorem, with the normalisation  $P(\hat{p}_\mu^R, E_\mu^R, E_{shw}^R, q_\nu^R) = 1$ , Eq. 2 can be re-written in the following way:

$$P = P(\hat{p}_\mu^R, E_\mu^R, E_{shw}^R, q_\nu^R | \hat{p}_\nu, E_\nu, q_\nu) \times P(\hat{p}_\nu, E_\nu, q_\nu), \quad (3)$$

where the term  $P(\hat{p}_\nu, E_\nu, q_\nu)$  is the Bayesian prior, and gives the expected distributions of  $\hat{p}_\nu$  and  $E_\nu$  for neutrinos and antineutrinos.

Eq. 3 is further modified by introducing PDFs relating the true and reconstructed event kinematics. The result is as follows:

$$P = P(\hat{p}_\mu^R, E_\mu^R, E_{shw}^R, q_\nu^R | \hat{p}_\mu, E_\mu, E_{shw}, q_\nu) \times P(\hat{p}_\mu, E_\mu, E_{shw} | \hat{p}_\nu, E_\nu, q_\nu) \times P(\hat{p}_\nu, E_\nu, q_\nu). \quad (4)$$

In Eq. 4, the first term, which is written as  $P(\hat{p}_\mu^R, E_\mu^R, E_{shw}^R, q_\nu^R | \hat{p}_\mu, E_\mu, E_{shw}, q_\nu)$ , contains a set of resolution functions connecting the reconstructed muon and shower kinematics to the underlying true muon and shower distributions. This term also contains the relative selection efficiency for atmospheric neutrinos as a function of energy. The second term,  $P(\hat{p}_\mu, E_\mu, E_{shw} | \hat{p}_\nu, E_\nu, q_\nu)$ , contains a set of kinematic distributions connecting the true muon and shower kinematics to the underlying neutrino interaction kinematics. This term incorporates the relative cross-sections and kinematic distributions for quasi-elastic (QE), resonance (RES), and deep-inelastic (DIS)  $\nu_\mu$  and  $\bar{\nu}_\mu$  CC interactions. The third term,  $P(\hat{p}_\nu, E_\nu, q_\nu)$ , is the Bayesian prior, described above. Taken together, the three terms combine the relative probability of an atmospheric neutrino interaction at a given energy and angle, with the distribution of kinematic observables produced by the neutrino interaction.

The following subsections describe the calculation of each of the terms in Eq. 4, along with the approximations made in their calculations.

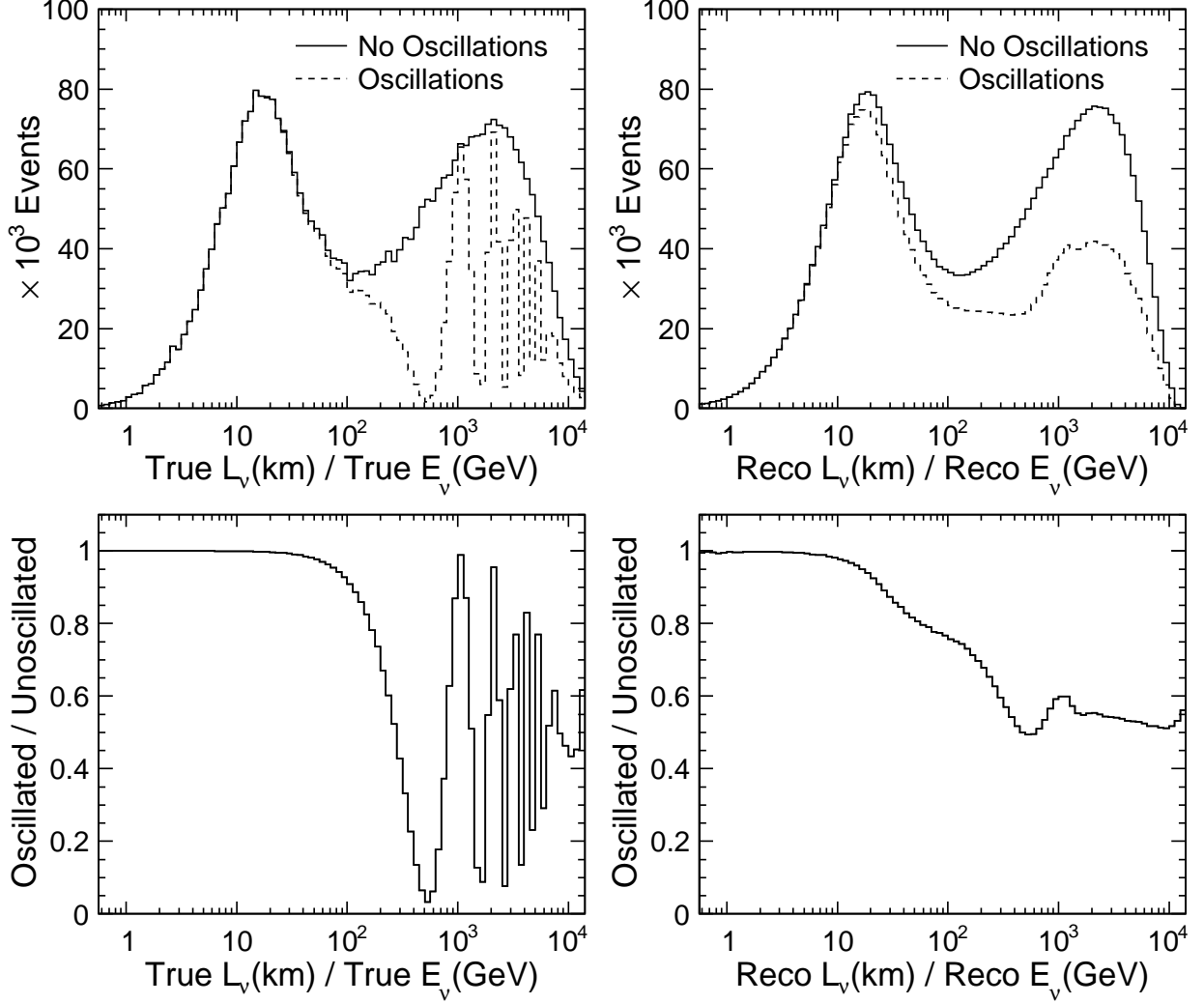


Figure 1: The top panels show the true and reconstructed  $L_\nu/E_\nu$  distributions for simulated contained-vertex atmospheric neutrinos in the MINOS detector. In each case, the solid line shows the prediction without oscillations and the dotted line shows the oscillated prediction, using representative oscillation parameters of  $\Delta m^2 = 2.32 \times 10^{-3} \text{eV}^2$  and  $\sin^2 2\theta = 1.0$ . The bottom panels show the ratios of the distributions calculated with and without oscillations. The first oscillation maximum is visible in the ratio of reconstructed  $L_\nu/E_\nu$  distributions as a dip at  $\log_{10}(L_\nu/E_\nu) \approx 2.7$ . However, at higher values of  $L_\nu/E_\nu$ , the oscillations are smeared out. (Note: the up-turn at very high  $L_\nu/E_\nu$ , where the lowest energy and hence shortest events occur, is due to an increased contamination of downward-going neutrinos mis-identified as upward-going neutrinos.)

### 3.1. Resolution Functions

The resolution functions translate the underlying distributions of true muon and shower variables into the distributions of reconstructed variables. To calculate the resolution functions, it is assumed that each observable is measured independently of the others. In this approximation, the resolution functions decouple into single-variable parameterisations. For the muon and shower energy, these are given by  $P(E_\mu^R|E_\mu)$  and  $P(E_{shw}^R|E_{shw}, q_\nu)$  respectively, where separate shower resolution functions are calculated for neutrinos and antineutrinos. For the muon direction, a perfect resolution is assumed. This is a reasonable approximation, since the average angular resolution of  $1 - 2$  degrees for reconstructed muon tracks is significantly smaller than the average angle between the neutrino and emitted muon. Therefore, the muon direction is fixed by setting  $P(\hat{p}_\mu^R|\hat{p}_\mu) = \delta(\hat{p}_\mu^R - \hat{p}_\mu)$ . For the muon charge-sign, the set of probabilities  $P(q_\nu^R|q_\nu)$  are approximated using a similar method. The atmospheric neutrino selection criteria are used to identify muons that have a well-measured curvature. For these events, a perfect charge-sign reconstruction is assumed, given by  $P(q_\nu^R|q_\nu) = \delta(q_\nu^R - q_\nu)$ . The vast majority of the contained-vertex events fall into this category. For those remaining events, it is assumed that  $P(q_\nu^R|q_\nu) = 1/2$ .

With these approximations, the overall resolution function can be written as follows:

$$\begin{aligned} &P(\hat{p}_\mu^R, E_\mu^R, E_{shw}^R, q_\nu^R | \hat{p}_\mu, E_\mu, E_{shw}, q_\nu) \\ &= \delta(\hat{p}_\mu^R - \hat{p}_\mu) \times P(q_\nu^R | q_\nu) \\ &\times P(E_\mu^R | E_\mu) \times P(E_{shw}^R | E_{shw}, q_\nu) \end{aligned} \quad (5)$$

To calculate  $P(E_\mu^R|E_\mu)$  and  $P(E_{shw}^R|E_{shw}, q_\nu)$ , the 5.2 million Monte Carlo events are used to populate 2D distributions in the reconstructed and true energy of muon tracks and hadronic showers. The distributions are then parameterised to create resolution functions that return a relative probability for each combination of reconstructed and true energy. For muon tracks, separate parameterisations are constructed for stopping and exiting muons, which correspond to fully contained and partially contained events, respectively. For hadronic showers, separate parameterisations are constructed for  $\nu_\mu$  CC QE,  $\nu_\mu$  CC RES+DIS,  $\bar{\nu}_\mu$  CC QE and  $\bar{\nu}_\mu$  CC RES+DIS neutrino interactions.

Fig. 2 shows a parameterisation of the average fractional resolutions as a function of true energy,

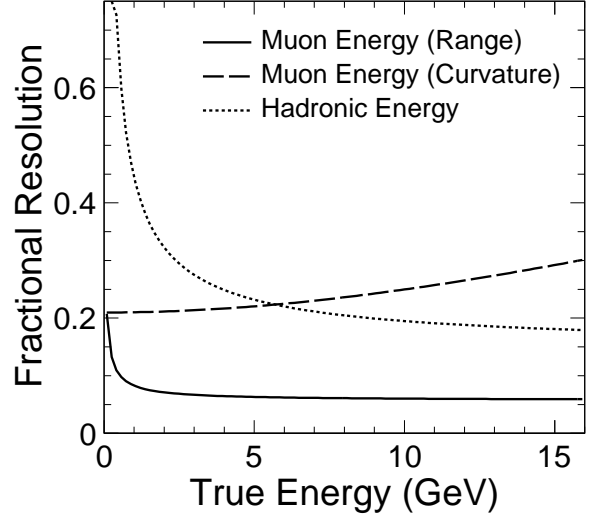


Figure 2: Parameterised energy resolution functions for reconstructed atmospheric neutrino  $\nu_\mu$  and  $\bar{\nu}_\mu$  CC interactions in the MINOS detector. The fractional energy resolutions are plotted as a function of the true energy for: the muon energy calculated from range for fully contained muons (solid line); the muon energy calculated from curvature for partially contained muons (dashed line); and the hadronic shower energy (dotted line).

for the muon energy, determined from either range or curvature, and for the hadronic shower energy. The resolutions are averaged over all the selected atmospheric neutrino  $\nu_\mu$  and  $\bar{\nu}_\mu$  CC interactions. For fully contained events, the muon energy is determined from track range with a typical resolution of a few percent. However, the muon energy from track curvature and the hadronic shower energy both have significantly worse resolutions. Therefore, the overall neutrino energy resolution is better for fully contained than partially contained events, and also better for neutrino interactions with smaller inelasticities.

### 3.2. Kinematic Distributions

A set of kinematic distributions are used to calculate PDFs of the true muon and shower observables for a given neutrino energy and direction. To construct the kinematic distributions, the NEUGEN simulation is used to generate a sample of 1 billion  $\nu_\mu$  and  $\bar{\nu}_\mu$  CC interactions with a uniform energy spectrum. The simulated interactions are separated into neutrinos and antineutrinos and are binned according to their interaction type (QE, RES, DIS). In each bin, a 3D PDF in neutrino energy,  $E_\nu$ , and the kinematic variables,  $W^2$  and  $y$ , is populated,

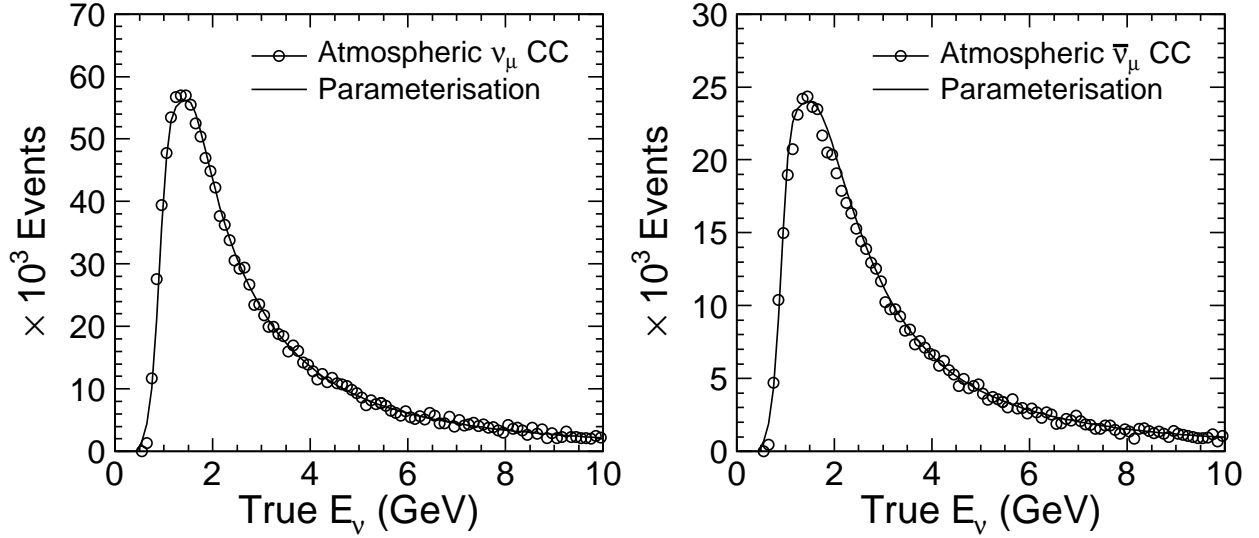


Figure 3: Distributions of true neutrino energy for Monte Carlo atmospheric  $\nu_\mu$  (left) and  $\bar{\nu}_\mu$  (right) CC interactions that satisfy the event selection cuts. In each plot, the open circles show the distributions of selected Monte Carlo events, and the solid line shows the parameterisations used as priors in the Bayesian L/E analysis. At low energies, the spectrum rises sharply as the selection efficiency increases rapidly from zero; at higher energies, the spectrum falls away, reflecting the underlying atmospheric neutrino energy spectrum.

where  $W^2$  is the invariant mass squared of the final-state hadronic system, and  $y$  is the inelasticity of the interaction. By neglecting the effects of Fermi momentum in the interactions, each combination of kinematic variables  $(E_\nu, W^2, y)$  can be mapped on to a single muon energy, hadronic energy, and relative angle between the neutrino and muon. Therefore, for a given neutrino energy and direction, PDFs of the true muons and shower observables  $(\hat{p}_\mu, E_\mu, E_{shw})$  can be calculated by marginalising the kinematic distributions over  $W^2$  and  $y$ , weighting each bin of interaction type according to its relative probability as a function of neutrino energy.

### 3.3. Bayesian Prior

The Bayesian prior gives the expected distributions in energy and angle for  $\nu_\mu$  and  $\bar{\nu}_\mu$  CC interactions. For the analysis presented here, the distributions are obtained from the Monte Carlo simulation. The expected energy distribution,  $P(E_\nu, q_\nu)$ , is found by calculating the product of the flux and total cross-section for neutrinos and antineutrinos. For the angular distribution, it is assumed that the incident flux of atmospheric neutrinos is isotropic. This is a reasonable approximation, since the selected events have an average energy of  $> 1$  GeV. In this energy region, the atmospheric  $\nu_\mu$  and  $\bar{\nu}_\mu$

flux is approximately uniform as a function of the neutrino zenith angle [18].

The energy distributions of  $\nu_\mu$  and  $\bar{\nu}_\mu$  CC interactions is combined with the selection efficiency,  $\epsilon^R(E_\nu, q_\nu)$ , which has a strong energy dependence. Fig. 3 shows the resulting energy distributions,  $P^R(E_\nu, q_\nu) = P(E_\nu, q_\nu) \times \epsilon^R(E_\nu, q_\nu)$ , for selected neutrinos and antineutrinos. These distributions are parameterised for the Bayesian  $L_\nu/E_\nu$  analysis. In each case, the distributions rise sharply at low energies, as the selection efficiency increases rapidly from zero; the distributions then fall away again at higher energies, reflecting the underlying atmospheric neutrino energy spectrum.

The calculated  $L_\nu/E_\nu$  resolutions are found to be insensitive to the exact choice of Bayesian prior, particularly the best  $L_\nu/E_\nu$  resolutions, where only a small region in neutrino energy and zenith angle contributes significantly to the Bayesian PDF. When a flat energy spectrum is used as a prior, similar results are obtained.

### 3.4. Calculating the Bayesian PDF

For each event, a posterior PDF in  $\log_{10}(L/E)$  is calculated by multiplying the resolution functions, kinematic distributions and Bayesian prior, and marginalising over the kinematic variables  $E_\nu$ ,

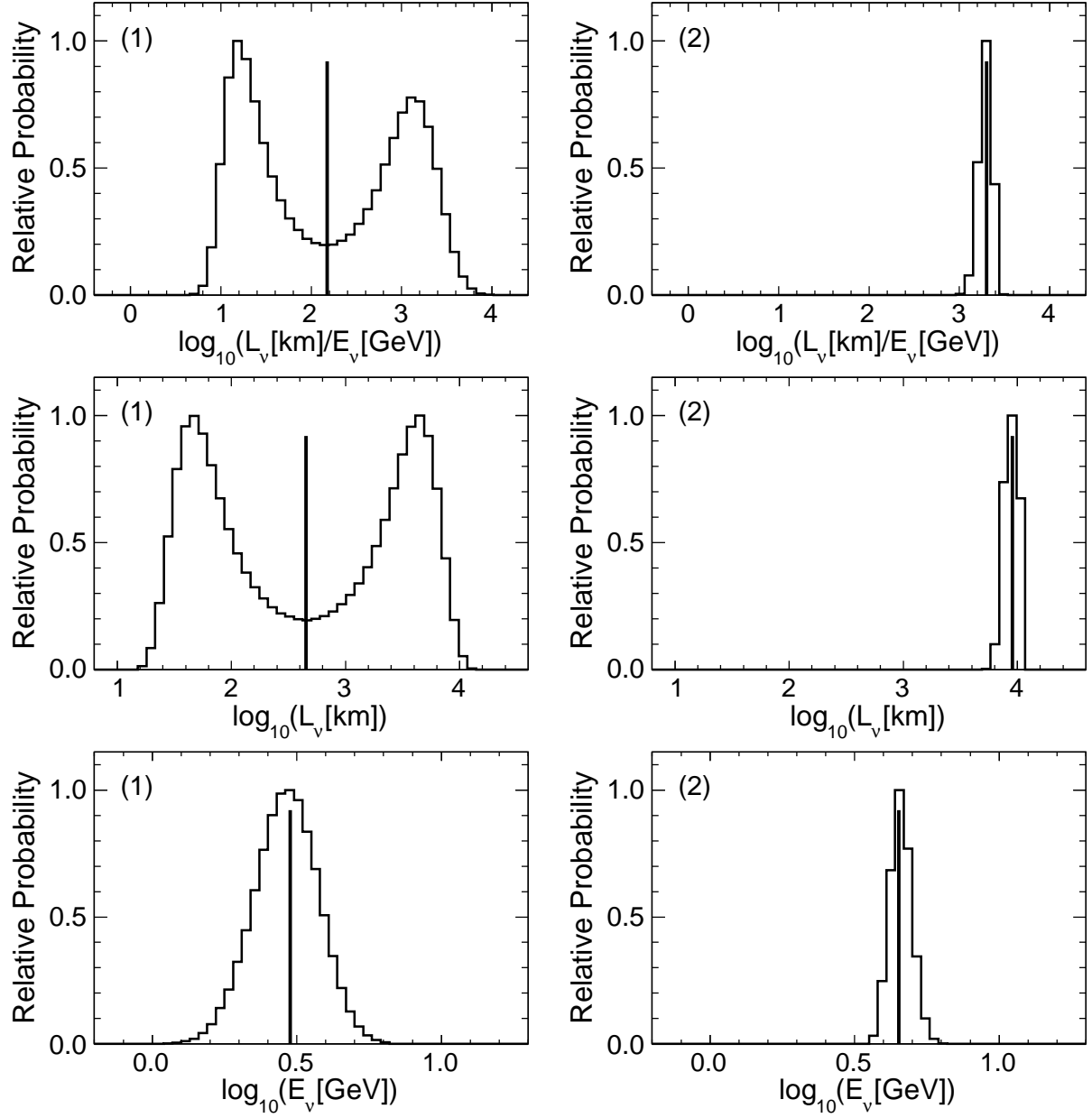


Figure 4: Examples of Bayesian PDFs in  $\log_{10}(L_\nu/E_\nu)$ ,  $\log_{10}(L_\nu)$  and  $\log_{10}(E_\nu)$  for two reconstructed atmospheric neutrinos. The left panels show a partially contained event with reconstructed energies of  $E_\mu^R = 2$  GeV and  $E_{shw}^R = 1$  GeV. The muon direction is perfectly horizontal and the charge-sign is negative. The  $L_\nu/E_\nu$  resolution is calculated to be  $\sigma_{\log(L_\nu/E_\nu)} = 0.87$ . The right panels show a fully contained event with reconstructed energies of  $E_\mu^R = 4$  GeV and  $E_{shw}^R = 0.5$  GeV. The muon direction is directed  $45^\circ$  upwards, and the charge-sign is positive. The  $L_\nu/E_\nu$  resolution is calculated to be  $\sigma_{\log(L_\nu/E_\nu)} = 0.07$ . In each plot, the vertical lines indicate the reconstructed values, and the histograms give the calculated PDFs.

$W^2$ ,  $y$ . At each point in this parameter space, the true muon momentum and hadronic energy is calculated, along with the relative angle between the muon and incident neutrino. The true muon direction is fixed on the reconstructed muon direction, and an additional integral is then performed over an angle,  $\phi$ , which rotates the neutrino around this direction. At each point in the integral, the true values of  $L_\nu$  and  $E_\nu$ , and therefore  $\log_{10}(L_\nu/E_\nu)$ , are calculated. A weight is assigned as given by the product of the input PDFs, and the value of  $\log_{10}(L_\nu/E_\nu)$  is entered into the posterior PDF with this weight. The values of  $\log_{10}(L_\nu)$  and  $\log_{10}(E_\nu)$  are entered into a separate set of PDFs, providing information on the relative resolution of  $L_\nu$  and  $E_\nu$  for each event. After the full PDF in  $\log_{10}(L_\nu/E_\nu)$  has been calculated, its RMS value, labelled  $\sigma_{\log(L_\nu/E_\nu)}$ , is taken as the  $L_\nu/E_\nu$  resolution of the event.

### 3.5. Examples

Fig. 4 shows examples of PDFs in  $\log_{10}(L_\nu)$ ,  $\log_{10}(E_\nu)$  and  $\log_{10}(L_\nu/E_\nu)$  for two reconstructed atmospheric neutrinos. The first event is a partially contained muon with reconstructed energies of  $E_\mu^R = 2\text{ GeV}$  and  $E_{shw}^R = 1\text{ GeV}$ . The reconstructed muon track direction,  $\hat{p}_\mu^R$ , is perfectly horizontal, and the reconstructed muon charge-sign is negative,  $q^R = -1$ , implying a  $\nu_\mu$  CC interaction. For this event, the resulting PDF in  $\log_{10}(L_\nu/E_\nu)$  has a double-peaked structure, arising from the rapid variation in the propagation distance,  $L_\nu$ , with the neutrino zenith angle close to the horizon. The resolutions on  $L_\nu$  and  $E_\nu$  are calculated to be  $\sigma_{\log(L_\nu)} = 0.86$  and  $\sigma_{\log(E_\nu)} = 0.11$ , respectively, and the overall resolution is  $\sigma_{\log(L_\nu/E_\nu)} = 0.87$ . This is an example of a low resolution event, where the broad  $\log_{10}(L_\nu)$  distribution makes the dominant contribution to the overall  $L_\nu/E_\nu$  resolution.

The second event is a fully contained muon that has reconstructed energies of  $E_\mu^R = 4\text{ GeV}$  and  $E_{shw}^R = 0.5\text{ GeV}$ . The reconstructed muon direction is directed upwards at an angle of  $45^\circ$  to the horizontal, and the reconstructed muon charge-sign is positive,  $q^R = +1$ , implying a  $\bar{\nu}_\mu$  CC interaction. Since the muon direction is significantly above the horizon, the variations in  $L_\nu$  as a function of zenith angle are small, giving a narrow PDF in  $\log_{10}(L_\nu)$ , with  $\sigma_{\log(L_\nu)} = 0.06$ . Since the event is fully contained, the neutrino energy is also well-measured and the PDF in  $\log_{10}(E_\nu)$  returns a small resolu-

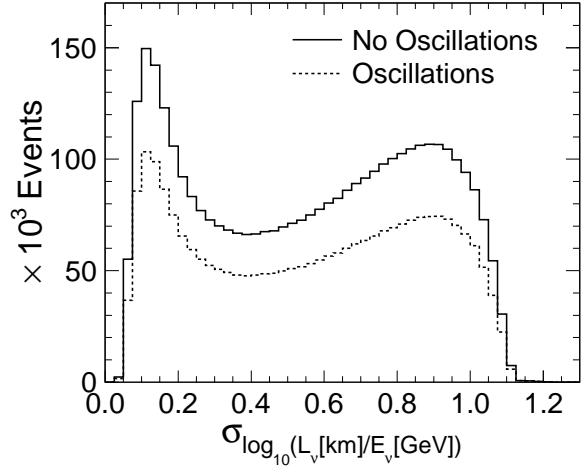


Figure 5: Distribution of Bayesian  $L/E$  resolution,  $\sigma_{\log(L/E)}$ , for the simulated atmospheric neutrino sample. The solid histogram shows the predicted distribution in the absence of oscillations; the dotted line shows the predicted distribution for representative oscillation parameters of  $\Delta m^2 = 2.32 \times 10^{-3} \text{ eV}^2$  and  $\sin^2 2\theta = 1.0$ .

tion of  $\sigma_{\log(E_\nu)} = 0.04$ . The two distributions combine to give a narrow PDF in  $\log_{10}(L_\nu/E_\nu)$ , with an overall  $L_\nu/E_\nu$  resolution of  $\sigma_{\log(L_\nu/E_\nu)} = 0.07$ . This is an example of a high resolution event.

## 4. Separation of Events by L/E Resolution

Fig. 5 shows the distribution of  $\sigma_{\log(L_\nu/E_\nu)}$  for the simulated event sample, plotted with and without oscillations. There is a substantial spread of  $\sigma_{\log(L_\nu/E_\nu)}$  values across the event sample, corresponding to  $\sim 25\%$  of the overall spread of the reconstructed neutrino  $\log_{10}(L_\nu/E_\nu)$  distribution. The lowest values of  $\sigma_{\log(L_\nu/E_\nu)}$  are roughly an order of magnitude smaller than the highest values. The shape of the predicted  $\sigma_{\log(L_\nu/E_\nu)}$  distribution is also approximately independent of oscillations.

To calculate oscillation sensitivities, the events are separated into bins of  $L_\nu/E_\nu$  resolution, using the two-bin, four-bin and eight-bin schemes given in Table 1. Fig. 6 shows the reconstructed distributions of  $\log_{10}(L_\nu/E_\nu)$  for the four-bin scheme, calculated with and without neutrino oscillations. Also shown are the ratios of the distributions with and without oscillations for each resolution bin. The oscillation dip is seen to become increasingly pronounced with improving resolution, and is most sharply defined in the bin with best resolution. Here, the ratio initially falls with  $\log_{10}(L_\nu/E_\nu)$ ,



Bin number	Two resolution bins	Four resolution bins	Eight resolution bins
1	$0.00 \leq \sigma_{\log(L/E)} < 0.50$	$0.00 \leq \sigma_{\log(L/E)} < 0.25$	$0.000 \leq \sigma_{\log(L/E)} < 0.125$
2	$0.50 \leq \sigma_{\log(L/E)} < 1.50$	$0.25 \leq \sigma_{\log(L/E)} < 0.50$	$0.125 \leq \sigma_{\log(L/E)} < 0.250$
3	—	$0.50 \leq \sigma_{\log(L/E)} < 0.75$	$0.250 \leq \sigma_{\log(L/E)} < 0.375$
4	—	$0.75 \leq \sigma_{\log(L/E)} < 1.50$	$0.375 \leq \sigma_{\log(L/E)} < 0.500$
5	—	—	$0.500 \leq \sigma_{\log(L/E)} < 0.625$
6	—	—	$0.625 \leq \sigma_{\log(L/E)} < 0.750$
7	—	—	$0.750 \leq \sigma_{\log(L/E)} < 0.950$
8	—	—	$0.950 \leq \sigma_{\log(L/E)} < 1.500$

Table 1: Binning schemes used to separate selected events according to the calculated  $L_\nu/E_\nu$  resolution.

reaching a first minimum at the point of maximum oscillation probability. As  $\log_{10}(L_\nu/E_\nu)$  increases, a second oscillation dip is clearly visible, before the ratio tends to an average value of  $1 - \frac{1}{2} \sin^2 2\theta = 0.5$ , as the frequency of the oscillations becomes rapid. Since the highest resolution bin contains a sample of events with a better resolved oscillation structure, the separation of events into bins of resolution is expected to yield a significant improvement in the oscillation sensitivity.

The shape of the  $\log_{10}(L_\nu/E_\nu)$  distribution in each  $L_\nu/E_\nu$  resolution bin reflects the underlying distribution of neutrino energies and angles. The events with worse resolution are associated with lower energies and angles closer to the horizon, whereas the events with higher resolution are associated with higher energies and steeper angles. Therefore, the central region of the  $\log_{10}(L_\nu/E_\nu)$  distribution, associated with horizontal neutrinos, is increasingly suppressed in higher resolution bins. The oscillation structure is most sharply resolved in multi-GeV upward-going events, which typically have the best  $L_\nu/E_\nu$  resolution.

## 5. Neutrino Oscillation Sensitivity Study

The impact of  $L_\nu/E_\nu$  resolution binning on the oscillation measurement is evaluated by performing a maximum likelihood analysis on the reconstructed  $\log_{10}(L_\nu/E_\nu)$  distributions. The projected oscillation sensitivity is calculated first without resolution binning, and then with resolution binning using the two-bin, four-bin and eight-bin schemes.

For this sensitivity study, the Monte Carlo distributions are scaled to an equivalent exposure of 37.9 kton-years, matching the analysis described in [11]. The selected events are binned according to their

reconstructed muon charge-sign,  $q=(\nu, \bar{\nu}, X)$ , corresponding to neutrinos ( $\nu$ ), antineutrinos ( $\bar{\nu}$ ) and those events with an ambiguous charge-sign ( $X$ ). Each bin of charge-sign is then separated into the required number of  $L_\nu/E_\nu$  resolution bins.

The oscillation sensitivities are calculated on a 2D grid in the oscillation parameters  $(\Delta m^2, \sin^2 2\theta)$ . At each grid point, the reconstructed  $\log_{10}(L_\nu/E_\nu)$  distributions are calculated using the selected Monte Carlo events. In addition, a set of predicted distributions are calculated using representative oscillation parameters of  $\Delta m^2 = 2.32 \times 10^{-3} \text{ eV}^2$  and  $\sin^2 2\theta = 1.0$ . These distributions are treated as simulated data, and used to evaluate the following negative log-likelihood function:

$$\begin{aligned}
-\ln \mathcal{L} = & \sum_q \mu - n \ln \mu \\
& - \sum_q \sum_{i,k} n_{ik} \ln(f_{ik}) \\
& + \sum_j \frac{\alpha_j^2}{2\sigma_{\alpha_j}^2}.
\end{aligned} \tag{6}$$

This log-likelihood function is divided into the following terms:

1. *Normalisation:* The sums  $\sum_q \mu - n \ln \mu$  represent the Poisson probability for observing  $n$  total events, with a total prediction of  $\mu$  events. The sum is taken over the charge-sign bins  $q=(\nu, \bar{\nu}, X)$ .
2. *Shape Term:* The terms  $\sum_q \sum_{i,k} n_{ik} \ln(f_{ik})$  represent the likelihood functions for each of the  $\log_{10}(L/E)$  distributions used in the fit. The  $i$ -sum is taken over the resolution bins; the  $k$ -sum is taken over the  $\log_{10}(L/E)$  bins.

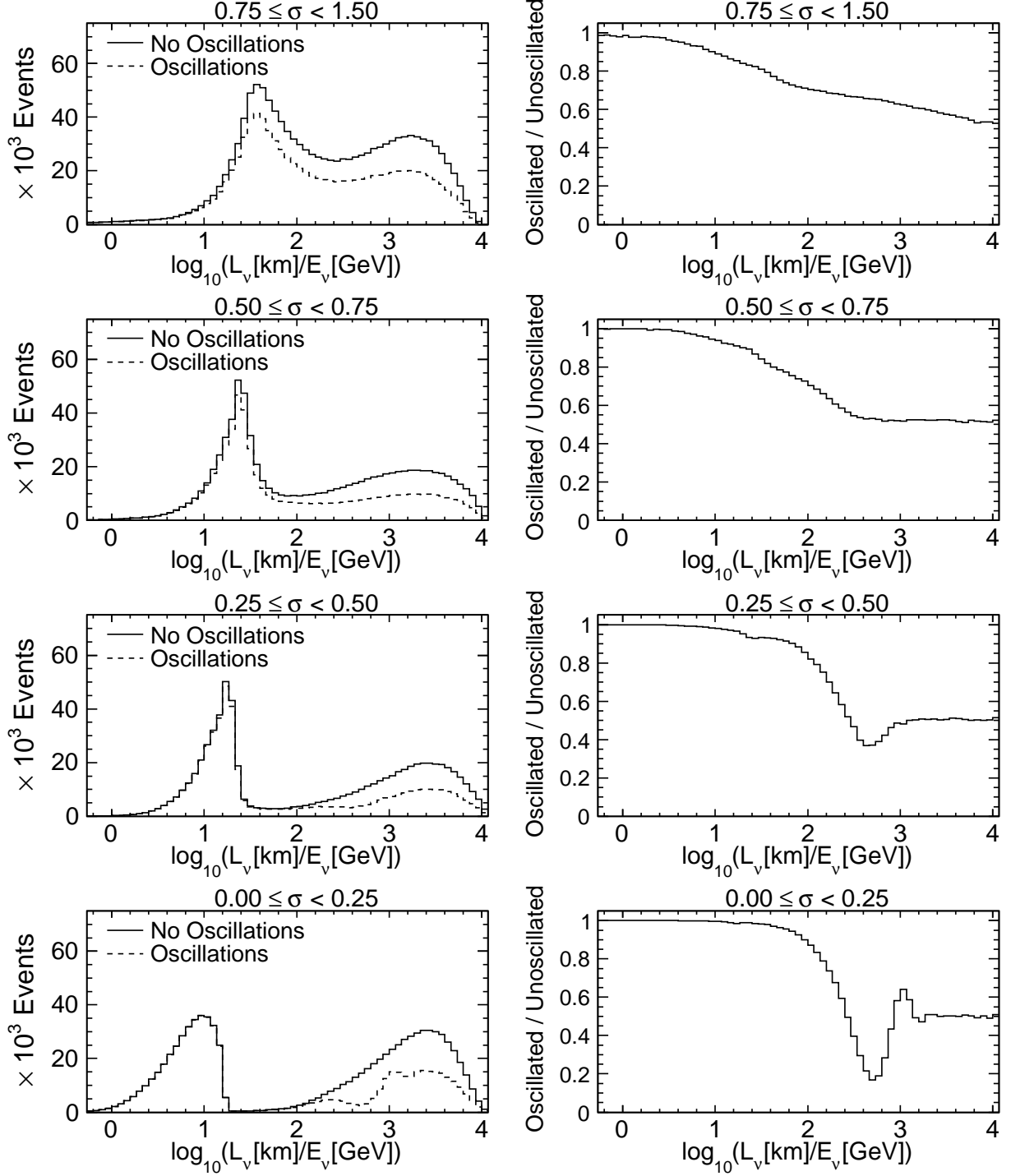


Figure 6: The left panels show the reconstructed  $\log(L/E)$  distributions for simulated atmospheric neutrinos, plotted with and without oscillations, and separated into the following four bins of resolution:  $0 < \sigma_{\log(L/E)} < 0.25$ ;  $0.25 < \sigma_{\log(L/E)} < 0.5$ ;  $0.5 < \sigma_{\log(L/E)} < 0.75$ ;  $0.75 < \sigma_{\log(L/E)} < 1.5$ . In each panel, the solid line indicates the prediction in the absence of oscillations, and the dotted line gives the prediction for representative oscillation parameters of  $\Delta m^2 = 2.32 \times 10^{-3} \text{ eV}^2$  and  $\sin^2 2\theta = 1.0$ . The right panels show the ratios of the Monte Carlo predictions with and without oscillations. The oscillation structure becomes increasingly clear for bins of higher resolution, and is most sharply defined in the bin with the highest resolution.

Within the sum,  $n_{ik}$  is the observed number of events and  $f_{ik}$  is the relative probability in the  $i^{th}$  and  $k^{th}$  bins.

3. *Systematic Error Term:* Systematic effects are incorporated as nuisance parameters, where the shift  $\alpha_j$  represents the deviation of the  $j^{th}$  systematic parameter from its nominal value. A set of penalty terms,  $\alpha_j^2/2\sigma_{\alpha_j}^2$ , are added, where the error  $\sigma_{\alpha_j}$  represents the estimated uncertainty in the  $j^{th}$  systematic parameter. A total of 10 systematic effects are included in the log-likelihood function, to account for systematic uncertainties in the atmospheric neutrino flux and cross-section calculations [11]. The log-likelihood function is minimised with respect to each of the systematic parameters.

By evaluating the log-likelihood function at each grid point, a likelihood surface is constructed in  $(\Delta m^2, \sin^2 2\theta)$  parameter space. The confidence levels (C.L.) on the oscillation parameters are then calculated assuming Gaussian statistics, where the two-parameter 68% C.L. and 90% C.L. are given by the locus of points with log-likelihood values of  $-\Delta \ln \mathcal{L} = (1.15, 2.30)$  relative to the central value at the input oscillation parameters.

Fig. 7 shows the resulting 90% C.L. contours, calculated without any resolution binning, and for the case of two, four and eight bins of resolution. The use of resolution binning is found to yield significant improvements in oscillation sensitivity, particularly for the  $\Delta m^2$  parameter. The sensitivity improves with each doubling in the number of resolution bins, with the improvements becoming smaller each time. A set of single-parameter 90% C.L. are calculated for each of the oscillation parameters and are found to improve from  $1.4 < |\Delta m^2|/10^{-3}\text{eV}^2 < 4.9$  and  $\sin^2 2\theta > 0.79$  without using resolution binning, to  $1.7 < |\Delta m^2|/10^{-3}\text{eV}^2 < 3.2$  and  $\sin^2 2\theta > 0.81$  for the case of eight bins of resolution.

## 6. Summary

For atmospheric neutrino  $\nu_\mu$  and  $\bar{\nu}_\mu$  CC interactions, the  $L_\nu/E_\nu$  resolution is crucially important in determining the sensitivity to oscillations, but varies significantly from event to event. This paper has described a Bayesian technique for estimating the  $L_\nu/E_\nu$  resolution on an event-by-event basis, which enables an event sample to be separated into bins of resolution. The technique has been demonstrated using simulated at-

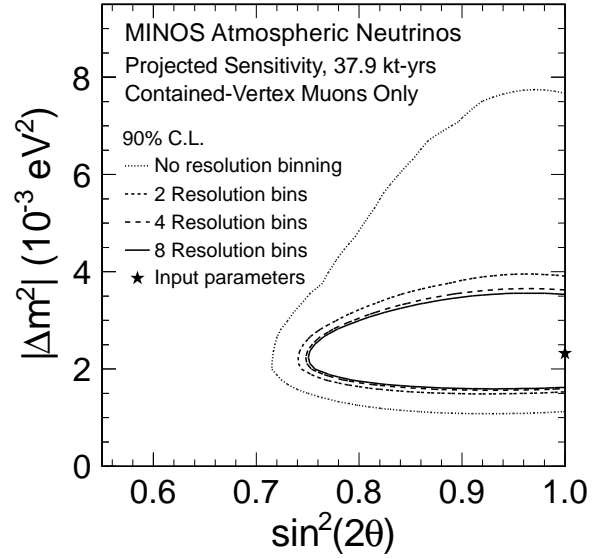


Figure 7: The projected 90% confidence limits on the oscillation parameters  $\Delta m^2$  and  $\sin^2 2\theta$ , calculated without resolution binning, and for the cases of two, four and eight bins of resolution. The sensitivities are calculated by scaling the contained-vertex atmospheric neutrino Monte Carlo sample to a total exposure of 37.9 kton-years. The input oscillation parameters are  $\Delta m^2 = 2.32 \times 10^{-3} \text{ eV}^2$  and  $\sin^2 2\theta = 1.0$ , as indicated by the star.

mospheric neutrino data from the MINOS experiment. The selected events are binned as a function of  $\log_{10}(L_\nu/E_\nu)$  and also by  $L_\nu/E_\nu$  resolution. The resolution binning takes full advantage of high resolution events, which sharply resolve the oscillations. It also allows low resolution events to be included in the analysis, which contribute to the oscillation sensitivity by providing information on the relative rate of upward-going and down-going neutrinos. By separating events into bins of  $L_\nu/E_\nu$  resolution, a significant improvement in the oscillation sensitivity can be achieved.

## Acknowledgements

The authors gratefully acknowledge the support of the MINOS collaboration and would like to thank Jon Urheim, Brett Viren and Anna Holin for their helpful suggestions and comments on this paper. This work was supported by the STFC, UK.

## References

- [1] B. Pontecorvo, JETP 34 (1958) 172.

- [2] V. N. Gribov and B. Pontecorvo, Phys. Lett. 28B (1969) 493.
- [3] Z. Maki, M. Nakagawa, and S. Sakata, Prog. Theor. Phys. 28 (1962) 870.
- [4] Y. Ashie *et al.* (Super-Kamiokande), Phys. Rev. Lett. 93 (2004) 101801.
- [5] Y. Ashie *et al.* (Super-Kamiokande), Phys. Rev. D 71 (2005) 112005.
- [6] K. Abe *et al.* (Super-Kamiokande), Phys. Rev. Lett. 97 (2006) 171801.
- [7] M. Ambrosio *et al.* (MACRO), Eur. Phys. J. C 36 (2004) 323.
- [8] W. W. M. Allison *et al.* (Soudan 2), Phys. Rev. D 72 (2005) 052005.
- [9] P. Adamson *et al.* (MINOS), Phys. Rev. D 73 (2006) 072002.
- [10] P. Adamson *et al.* (MINOS), Phys. Rev. D 75 (2007) 092003.
- [11] P. Adamson *et al.* (MINOS), arXiv:1208.2915 [hep-ex] (Submitted to Phys. Rev. D).
- [12] M. H. Ahn *et al.* (K2K), Phys. Rev. D 74 (2006) 072003.
- [13] D. G. Michael *et al.* (MINOS), Phys. Rev. Lett. 97 (2006) 191801.
- [14] P. Adamson *et al.* (MINOS), Phys. Rev. Lett. 101 (2008) 131802.
- [15] P. Adamson *et al.* (MINOS), Phys. Rev. Lett. 106 (2011) 181801.
- [16] K. Abe *et al.* (T2K), Phys. Rev. D 85 (2012) 031103.
- [17] D. G. Michael *et al.* (MINOS), Nucl. Instrum. Methods A 596 (2008) 190.
- [18] G. D. Barr *et al.*, Phys. Rev. D 70 (2004) 023006.
- [19] H. Gallagher, Nucl. Phys. B. Proc. Suppl. 112 (2002) 118.
- [20] S. Giani *et al.*, GEANT Detector Description and Simulation Tool, CERN Program Library Long Writeup, Report No. W5013 (unpublished).
- [21] A. Blake, PhD thesis, University of Cambridge (2005).
- [22] J. Marshall, PhD thesis, University of Cambridge (2008).
- [23] J. Chapman, PhD thesis, University of Cambridge (2007).